J. Fluid Mech. (2013), *vol.* 732, *pp.* 332–344. © Cambridge University Press 2013
doi:10.1017/jfm.2013.400

Vortex development on pitching plates with lunate and truncate planforms

Colin Hartloper and David E. Rival†

Department of Mechanical Engineering, University of Calgary, Calgary, AB T4N 1N4, Canada

(Received 4 March 2013; revised 23 July 2013; accepted 30 July 2013;
first published online 4 September 2013)

The three-dimensional flow field and instantaneous forces are measured on pitching rectangular, lunate and truncate planforms of aspect-ratio four. The leading-edge vortex on the rectangular planform is compressed as it grows, and subsequently forms an arch-shaped vortex. For the lunate and truncate planforms, which both have identical spanwise leading-edge curvature but differ in planform area, outboard-directed convection of vorticity, rather than vortex stretching, mitigates arch-vortex formation. The vortical near wake that is formed by the planforms with spanwise leading-edge curvature is found to be strongly correlated with a favourable lift-to-drag ratio during the force-relaxation phase.

Key words: separated flows, swimming/flying, vortex dynamic

1. Introduction

On at least four completely separate occasions, evolution has converged on lunate-shaped planforms for hydrodynamic propulsion: lamnid sharks, scombroids, cetaceans as well as ichthyosaurs. This process of evolutionary convergence implies that lunate-shaped planforms might be optimized for both efficient-cruise as well as high-acceleration conditions. Lighthill (1969) proposed that the caudal fin of carangiform swimmers had evolved a lunate shape to structurally cope with high thrust generation. Conversely, a recent study by Eloy (2013) employed a genetic algorithm that, independent of structural restraints, converged on a geometry with a lunate-like caudal fin when minimizing the energetic cost of undulatory swimming. However, this latter study did not explicitly account for the generation and shedding of vorticity, which, as shown by Gazzola, Van Rees & Koumoutsakos (2012), plays an important role in the high-acceleration motions necessary for both predation and escape manoeuvres. Thus, as suggested in Triantafyllou (2012), when considering high-acceleration motions, further investigation into the influence of appendage geometry on the resulting vortical wake is still required.

While recent studies by Lentink & Dickinson (2009) and Harbig, Sheridan & Thompson (2013) have illustrated the role that rotation plays in the stabilization of the leading-edge vortex (LEV), the exact influence of spanwise leading-edge curvature on vortex development in rectilinear motions, similar to the pitching of a caudal fin, has not been characterized in detail. Taira & Colonius (2009) studied impulsively-towed rectangular, semi-circular and elliptical planforms at Reynolds numbers of

† Email address for correspondence: derival@ucalgary.ca

https://doi.org/10.1017/jfm.2013.400 Published online by Cambridge University Press

$Re = 300$ and concluded that providing spanwise curvature about the leading edge promoted the convective transport of vorticity towards the tips, thus delaying LEV separation. However, when comparing the unsteady vortex growth on pitching elliptical and rectangular planforms of aspect-ratio two at $Re = 10\,000$, Yilmaz & Rockwell (2012) observed that an LEV eruption occurred at the midspan of both elliptical and rectangular planforms. In addition, Granlund, Ol & Bernal (2011) concluded that differences in both the forces and flow field on rectangular and Zimmerman planforms undergoing a rapid-pitching manoeuvre were minimal. As such, outstanding questions regarding the mechanisms by which spanwise leading-edge curvature influences vortex development remain unanswered.

In the present work, it is hypothesized that spanwise leading-edge curvature can stabilize the vortex growth on planforms via two possible mechanisms. The first mechanism is based on the promotion of convective transport of vorticity into the wake, which stabilizes the LEV on a delta-wing, as described by Maxworthy (2007). This convective transport is caused by an outward-directed flow that is induced in the LEV core via the angle between the oncoming flow velocity vector and the tangent of the leading edge. The second mechanism relies on LEV stretching. The vortex stretching/tilting vector ($\boldsymbol{W} = (\boldsymbol{\omega} \cdot \nabla)\boldsymbol{u}$) can be broken into components of stretching ($\boldsymbol{W}_{\parallel}$) and tilting ($\boldsymbol{W}_{\perp}$), which are parallel and perpendicular to the vorticity vector ($\boldsymbol{\omega}$), respectively. As outlined by Kinzel *et al.* (2011), positive and negative alignment between $\boldsymbol{\omega}$ and $\boldsymbol{W}_{\parallel}$ implies vortex stretching and compression, respectively. From Yilmaz & Rockwell (2012), the LEV eruption was correlated with inboard-directed spanwise velocities as well as a concentration of spanwise vorticity at the symmetry plane. The interaction of inboard-directed spanwise velocities at the symmetry plane would thus produce a large spanwise gradient in spanwise velocity, and this gradient would be negatively aligned with the spanwise vorticity. Therefore, it is proposed here that vortex compression is correlated with the LEV eruption process. Thus, if the leading edge is shaped so as to provide LEV stretching to counteract the vortex compression described above, it is hypothesized that LEV eruption could be mitigated.

Since an outboard-directed spanwise velocity is required for LEV stretching, both mechanisms for LEV stabilization hypothesized above can be tested by shaping the leading edge to induce LEV stretching. Based on the findings of LEV growth on an elliptical planform by Yilmaz & Rockwell (2012), it is assumed that the LEV vector remains parallel to the leading edge during the vortex-formation process. Then, as shown in figure 1, outboard-directed spanwise flow (u_t) will be induced in the LEV proportional to the projection of the oncoming velocity ($\boldsymbol{U}_\infty$) onto the instantaneous tangent ($\boldsymbol{\tau}$) of the leading edge:

$$u_t = \boldsymbol{U}_\infty \cdot \boldsymbol{\tau} = (U_\infty \boldsymbol{i}) \cdot \left(\frac{\partial x}{\partial s}\boldsymbol{i} + \frac{\partial z}{\partial s}\boldsymbol{k} \right) = U_\infty \frac{\partial x}{\partial s}, \tag{1.1}$$

where ∂s is an infinitesimal section of the leading-edge arc (s):

$$\partial s = \sqrt{1 + \left(\frac{\partial z}{\partial x} \right)^2}\, \partial x. \tag{1.2}$$

As only velocity gradients parallel to the leading edge will contribute to LEV stretching, the axial velocity gradient $\partial u_t / \partial s$ defines the LEV stretching. In order to control the level of stretching imposed on the LEV, it is desirable that the axial-

https://doi.org/10.1017/jfm.2013.400 Published online by Cambridge University Press

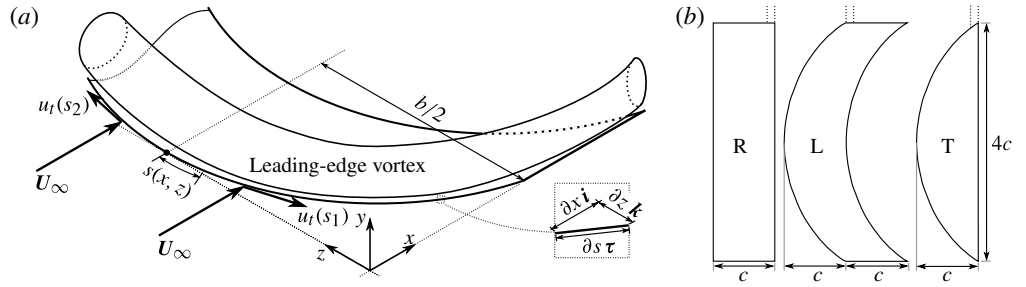


FIGURE 1. (*a*) Axial velocity (s) induced in the LEV is proportional to the projection of oncoming velocity ($\boldsymbol{U}_\infty$) on the tangent vector ($\boldsymbol{\tau}$) of the leading edge. (*b*) Rectangular (R), lunate (L), and truncate (T) planforms, with the sting mounting indicated by the dashed lines.

velocity gradient is held constant (A) throughout the LEV such that:

$$\frac{\partial u_t}{\partial s} = A. \tag{1.3}$$

By solving (1.1), (1.2) and (1.3) simultaneously, the relationship defining the leading-edge shape $z(x)$ becomes:

$$z(x) = \frac{b}{2} \pm \frac{1}{2A}\left[U_\infty \tan^{-1}\left(\frac{\sqrt{2Ax}}{\sqrt{U_\infty - 2Ax}}\right) + \sqrt{2Ax}\sqrt{U_\infty - 2Ax}\right], \tag{1.4}$$

where b is the planform's span. In order to test the influence of spanwise leading-edge curvature on the vortex growth and interactions, a comparison was conducted between three distinct planform shapes, as shown in figure 1. An aspect-ratio four rectangular (R) plate was used as a baseline for comparison to lunate (L) and truncate (T) planforms.

2. Experimental methods

Experiments were performed in a free-surface water tunnel with a mean width of 385 mm and water depth of 432 mm. The free-stream velocity of the water tunnel was set to $U_\infty = 0.1$–0.2 m s^{-1}, providing a chord-based Reynolds-number range of $Re = 5000$–$10\,000$, a range where Barnes & Visbal (2012) have shown that both the aerodynamic loads and flow field development on low-aspect-ratio plates are insensitive to Re. All three planforms were constructed from 3 mm-thick aluminium with spans of 200 mm and root chords of $c = 50$ mm, giving aspect ratios of four. All three planforms were pitched about the leading edge at three pitch rates for a total of nine test cases. The kinematics consisted of a sinusoidal pitch-up motion from a geometric angle of attack of $\alpha = 0$ to 45° in dimensionless times of $t^* = tU_\infty/c = 6, 4$ and 2 resulting in reduced frequencies of $k = \pi f\, c/U_\infty = 0.25, 0.4$ and 0.8, respectively. At $\alpha = 45°$ blockage is 4 %, and therefore blockage effects are neglected in the analysis.

Figure 2 elucidates the experimental apparatus. A 6.3 mm diameter stainless steel sting is arranged such that the plate is vertically centred in the water tunnel. See figure 1 for the sting mounting positions for all three planforms. An ATI Gamma six-component force and moment sensor placed at the base of the sting holding the plate was used to measure the instantaneous forces throughout the pitching motion.

https://doi.org/10.1017/jfm.2013.400 Published online by Cambridge University Press

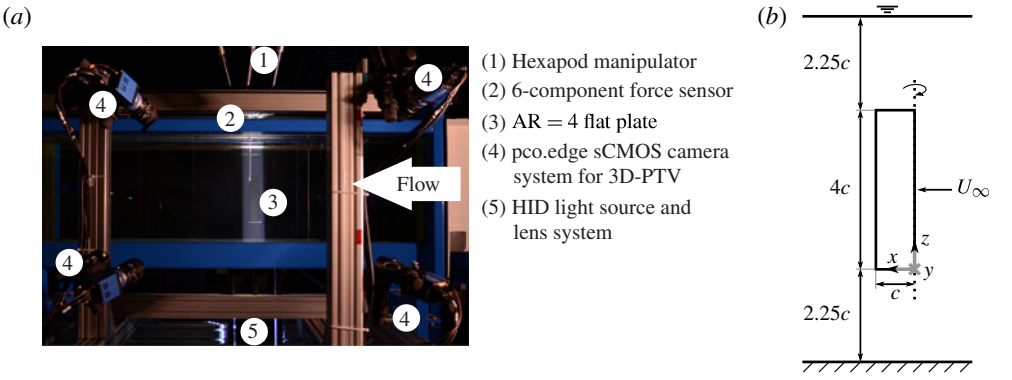


FIGURE 2. (Colour online) (*a*) Water tunnel test section with measurement system components. (*b*) Rectangular plate at $\alpha = 0°$, shown in reference to the fixed coordinate system as well as the water tunnel surface and floor. Note that the *y*-direction is positive out of the page.

Treatment of the raw force signals measured during each run, including the dynamic tare of the sting assembly, is similar to the procedure used in Hartloper, Kinzel & Rival (2013), after which the force data from 10 runs were averaged prior to the calculation of force coefficients for each test case. The three-dimensional particle-tracking velocimetry (3D-PTV) technique, as described by Luethi, Tsinober & Kinzelbach (2005), was used to quantify the flow field on the suction side of the pitching plates. Illumination of the measurement volume was provided by a high-intensity discharge (HID) light source columnated through a lens system consisting of a 40 mm and a 300 mm converging lens. The resulting 3D-PTV measurement volume had dimensions of 80 mm × 80 mm × 175 mm, with the longest dimension aligned with the span of the plate. Thus, the measurement volume spanned from $1c$ outboard of the tip to $2.5c$ inboard of the tip. During the experiments data were recorded with four pco.edge sCMOS cameras operated at a frame rate of 165 Hz and a resolution of 2560 pixel × 1280 pixel. Each test case was repeated 10 times and the constructed Lagrangian particle tracks were merged in a single data file, resulting in an average interparticle spacing of 3 mm. The Lagrangian velocities and accelerations were derived by differentiation of the particle tracks, and the Eulerian velocity derivatives were subsequently calculated from weighted interpolations of the Lagrangian data in a sphere around every data point. The velocity and velocity derivatives were then interpolated onto an Eulerian grid with a grid spacing of 5 mm. The normalized uncertainties in the *x*-, *y*- and *z*-velocity derivatives were estimated through a comparison of the Eulerian and Lagrangian accelerations. These normalized uncertainties were calculated to be 6 %, 5 % and 8 % of the *x*-, *y*-, and *z*-components of acceleration, respectively.

3. Results and discussion

The two mechanisms identified in § 1 by which spanwise leading-edge curvature was hypothesized to influence vortex development, namely vortex convection and vortex stretching, are addressed below. First, in § 3.1 trends in the force histories on the three planforms identify a temporal range where the forces, and hence the flow fields, deviate significantly due to spanwise leading-edge curvature. Next,

https://doi.org/10.1017/jfm.2013.400 Published online by Cambridge University Press

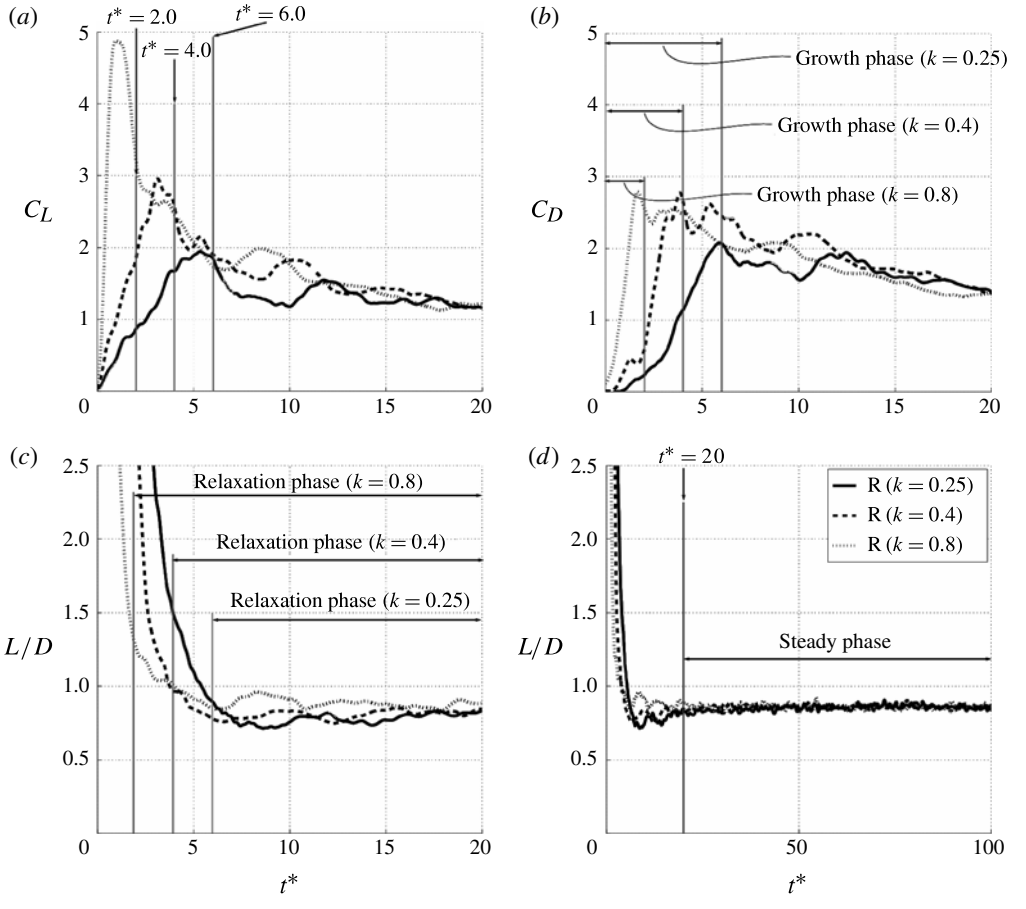


FIGURE 3. Force coefficients for the rectangular planform: (*a*) lift coefficient; (*b*) drag coefficient; (*c,d*) lift-to-drag ratio. The growth and relaxation phases (pitching period) are identified for all three reduced frequencies ($k = \pi fc/U_\infty$) and the end of the relaxation phase is identified at $t^* = tU_\infty/c = 20$.

in § 3.2 Lagrangian particle tracks contrast the vortical structures that arise in the presence or absence of spanwise leading-edge curvature, while an Eulerian approach is taken to demonstrate the significance of the convection of vorticity on such vortical structures. Finally, in § 3.3 the impact of vortex stretching and compression on the development of the vortical structures is assessed. In the following, the lift (C_L) and drag (C_D) coefficients are non-dimensionalized by U_∞ and planform area, while the z-velocity (w), vorticity, vortex stretching vector and LEV circulation (Γ_{LEV}) are all non-dimensionalized by the appropriate combination of U_∞ and c.

3.1. *Instantaneous forces*

In figure 3, three distinct phases can be identified on the rectangular planform and at all three reduced frequencies: a growth phase, a relaxation phase, and a steady phase. In the growth phase, the forces rapidly increase to a primary force peak in phase with the pitch acceleration. The period of the growth phase corresponds with the period of the pitching motion, such that the growth phase has a period of $t^* = 6, 4$ and 2

https://doi.org/10.1017/jfm.2013.400 Published online by Cambridge University Press

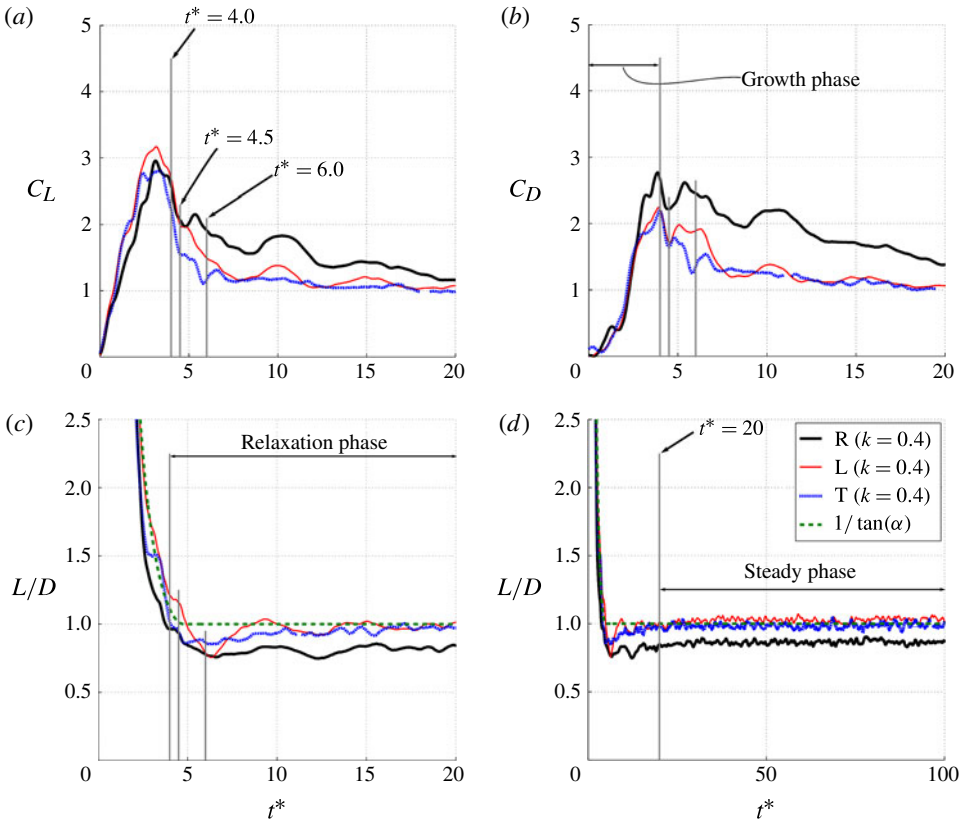


FIGURE 4. (Colour online) The growth phase for $k = 0.4$ ($t^* < 4$) is characterized by close agreement between the forces on all three planforms. During the relaxation phase ($4 < t^* < 20$), however, forces relax at a faster rate and maintain a higher L/D ratio in the presence of spanwise leading-edge curvature. Note that the L/D would be $1/\tan(\alpha)$ if the total force on the plate was directed normal to the plate surface.

for $k = 0.25, 0.4$ and 0.8, respectively. Note that the magnitude of the primary force peak increases with reduced frequency, while at the completion of the pitching motion the forces begin to relax to the steady-state values, reaching within 20 % of their steady-state values by $t^* = 20$.

In figure 4 it is observed that, for $k = 0.4$, there is close agreement between the forces on all three planforms during the growth phase ($t^* < 4$); note that R, L and T denote rectangular, lunate and truncate planforms. This trend is consistent across the reduced frequencies tested in the current study (see figures 5 and 6), which implies that during the pitching motion, while the plate is accelerating, the fluid reaction force is only a function of the kinematics. This planform-shape independence of forces on pitching plates is supported by results presented in Granlund *et al.* (2011).

During the relaxation phase ($4 < t^* < 20$), however, the forces are largely dependent on spanwise leading-edge curvature. Here the forces relax at a slower rate on the rectangular planform compared to the planforms with spanwise leading-edge curvature. Furthermore, the lift-to-drag ratio, L/D, is as much as 0.15 higher on the planforms with spanwise leading-edge curvature. To investigate if the flow field, similar to the forces, is largely dependent on spanwise leading-edge curvature,

https://doi.org/10.1017/jfm.2013.400 Published online by Cambridge University Press

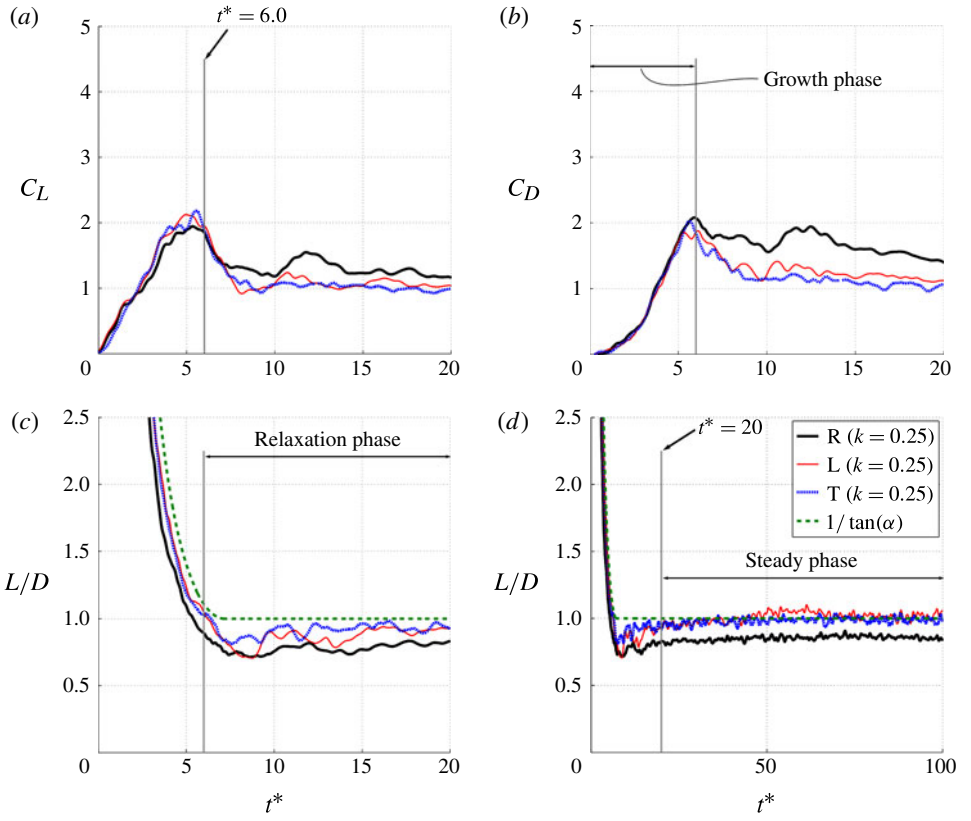


FIGURE 5. (Colour online) Similar to the results shown in figure 4, the growth phase for $k = 0.25$ ($t^* < 6$) is characterized by close agreement between the forces on all three planforms. However, during the relaxation phase ($6 < t^* < 20$), forces decay more slowly on the rectangular planform, and the L/D ratio is significantly lower on the rectangular planform compared to the planforms with spanwise leading-edge curvature.

3D-PTV measurements were performed on all three planforms at $k = 0.4$. In the presentation of the flow field measurements attention is given to the two time steps identified in figure 4. The first time step is $t^* = 4.5$, where the forces, especially the drag, begin to show a dependence on spanwise leading-edge curvature. The second time step is $t^* = 6$, where the forces have further decayed on the planforms with spanwise leading-edge curvature while remaining higher on the rectangular planform.

3.2. *Flow-field development*

In figure 7, Lagrangian particle tracks reveal that on the rectangular planform, similar to the results from Hartloper *et al.* (2013), the LEV and tip vortex (TV) remain distinct throughout the pitch-up motion from 0 to 45°. Furthermore, an arch-shaped vortex, as described by Yilmaz & Rockwell (2012) and Visbal, Yilmaz & Rockwell (2013), is observed to form in the times between $t^* = 3.0$ and $t^* = 4.5$. This arch-shaped LEV is further illustrated in figure 8, where it is revealed that at $t^* = 4.5$ the LEV has erupted from its feeding shear layer at the midspan. The flow field development on the lunate and truncate planforms contrasts with that of

https://doi.org/10.1017/jfm.2013.400 Published online by Cambridge University Press

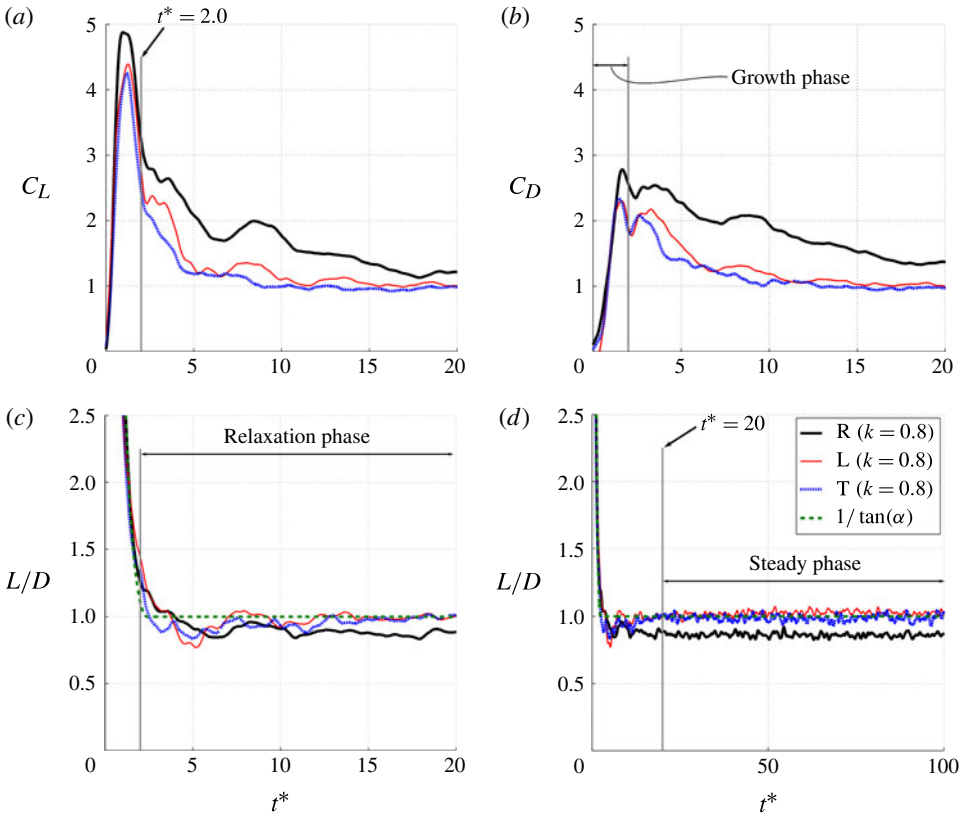


FIGURE 6. (Colour online) The trends in the force histories for $k = 0.8$ are similar to the trends for $k = 0.25$ and $k = 0.4$ as shown in figures 4 and 5, respectively.

the rectangular planform, where neither LEV eruption nor arch-vortex formation is observed at $t^* = 4.5$ nor throughout the relaxation phase.

In § 1 it was hypothesized that outboard-directed flow induced by spanwise leading-edge curvature could alter vortex development via the convection of vorticity towards the tip. To measure the contribution of convection towards vortex development, the LEV circulation (Γ_{LEV}) and average z-velocity ($\bar{w}$) are calculated through area integrations of counter-clockwise ω_z and w, respectively, on spanwise planes spaced between the tip and midspan. In figure 9, time histories of $\bar{w}^*$ reveal that inboard-directed flow is higher during the growth phase in the absence of spanwise leading-edge curvature. Thus z-vorticity is convected from the tip towards the midspan, resulting in the slower growth of Γ^*_{LEV} in the tip region of the rectangular planform shown in figure 8. The inboard-convected z-vorticity is subsequently tilted into xy-vorticity ($\omega^*_{xy} = (\omega_x^2 + \omega_y^2)^{0.5}$) on the rectangular planform, ultimately giving rise to the arch-shaped LEV. Since the leading edge is perpendicular to the z-axis, xy-vorticity can only be produced via vortex tilting in the inboard regions of the planform. High levels of xy-vorticity, with magnitudes on the same scale as z-vorticity, are found to persist throughout the relaxation phase in the inboard regions of the rectangular planform (see movie S1 of the supplementary material available at http://dx.doi.org/10.1017/jfm.2013.400), while such high levels are absent on the planforms with spanwise

https://doi.org/10.1017/jfm.2013.400 Published online by Cambridge University Press

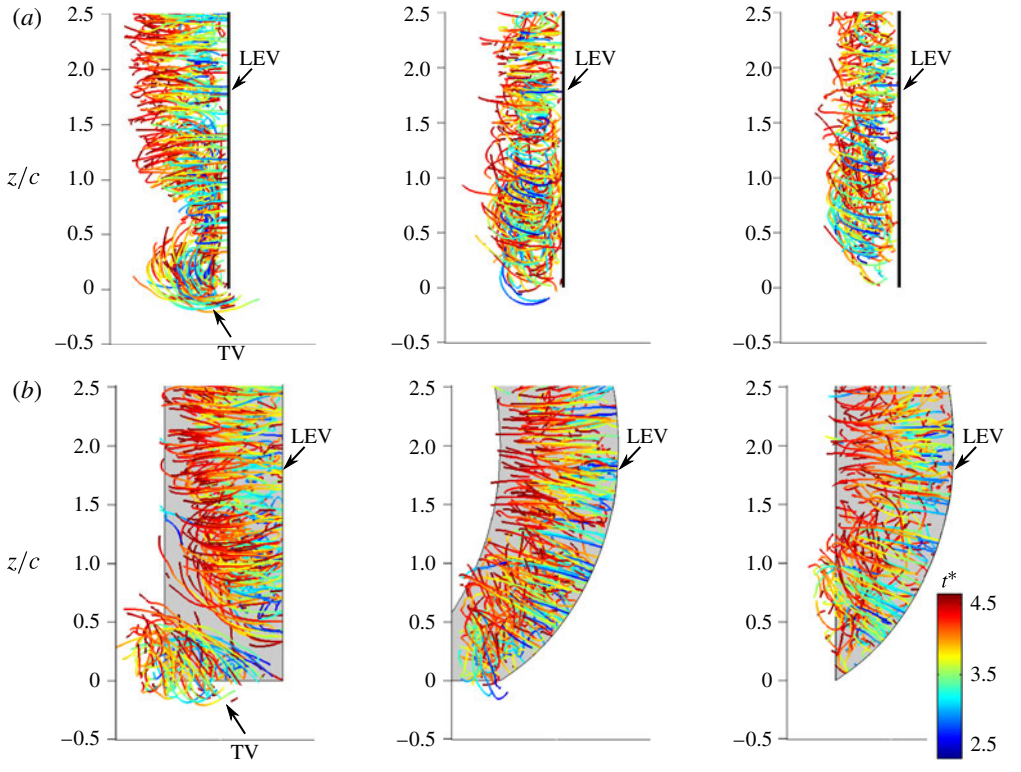


FIGURE 7. (Colour online) (*a*) Downstream views of Lagrangian particle tracks that are coloured by t^* and filtered such that only tracks with an average $|\omega|^* > 3.75$ are shown. Rectangular, lunate and truncate planforms, from left to right, are shown at $\alpha = 45°$. Note the development and suppression of the arch-shaped vortex in the presence or absence of spanwise leading-edge curvature. (*b*) Plate-normal views of particle tracks reveal the clear separation between the LEV and TV on the rectangular planform.

leading-edge curvature. This modification of the vortical near-wake on planforms with spanwise leading-edge curvature is strongly correlated with a favourable L/D ratio observed on the lunate and truncate planforms during the relaxation phase, as shown in figure 4.

3.3. *Vortex stretching and compression*

In § 1 it was hypothesized that the suppression of vortex compression could mitigate arch-vortex formation. To investigate if this is in fact the case, $W_{\parallel}$ is calculated at each Eulerian data point by a projection of $\boldsymbol{W}$ onto $\boldsymbol{\omega}$, where positive and negative $W_{\parallel}$ correspond to vortex stretching and compression, respectively. Isosurfaces of $W_{\parallel}$ are plotted in figure 10, where it is revealed that during the growth phase the LEVs on all three planforms are subject to vortex compression. It is suspected that the universality of vortex compression is due to the presence of a tip vortex on all three planforms during the growth phase, as the tip vortex would create a spanwise velocity gradient anti-parallel to the leading-edge vorticity. The trend of LEV compression continues on all three planforms as the arch-vortex grows or is suppressed in the presence or absence of spanwise leading-edge curvature. It is thus concluded that outboard-directed

https://doi.org/10.1017/jfm.2013.400 Published online by Cambridge University Press

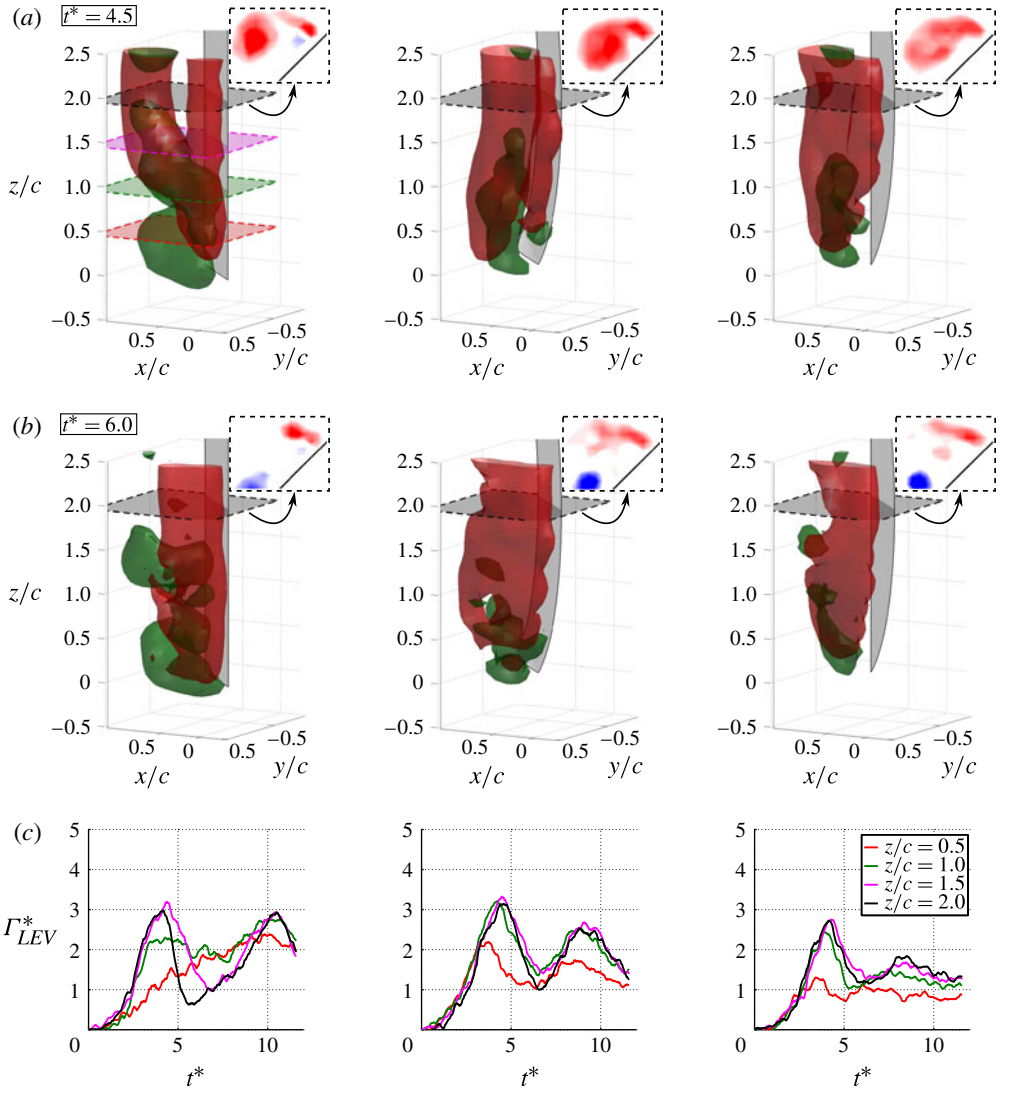


FIGURE 8. (Colour online) (*a*) Iso-surfaces of $\omega_z^* = 2.5$ (red), $\omega_{xy}^* = 2.5$ (green) and midspan iso-contours of ω_z^* at $t^* = 4.5$ highlight the formation of the arch-shaped vortex on the rectangular planform, contrasting the vortex development on the lunate and truncate planforms (rectangular, lunate and truncate planforms are shown from left to right). (*b*) High levels of ω_{xy}^* persist throughout the relaxation phase in the inboard regions of the rectangular planform. (*c*) The near-tip growth of Γ^*_{LEV} is slower in the absence of spanwise leading-edge curvature, while near the midspan Γ^*_{LEV} grows independent of spanwise leading-edge curvature.

vortex convection rather than LEV stretching is responsible for the mitigation of the arch vortex on planforms with spanwise leading-edge curvature.

4. Conclusions

Force measurements on pitching rectangular, lunate and truncate planforms at three reduced frequencies have identified three distinct time phases in the force histories:

https://doi.org/10.1017/jfm.2013.400 Published online by Cambridge University Press

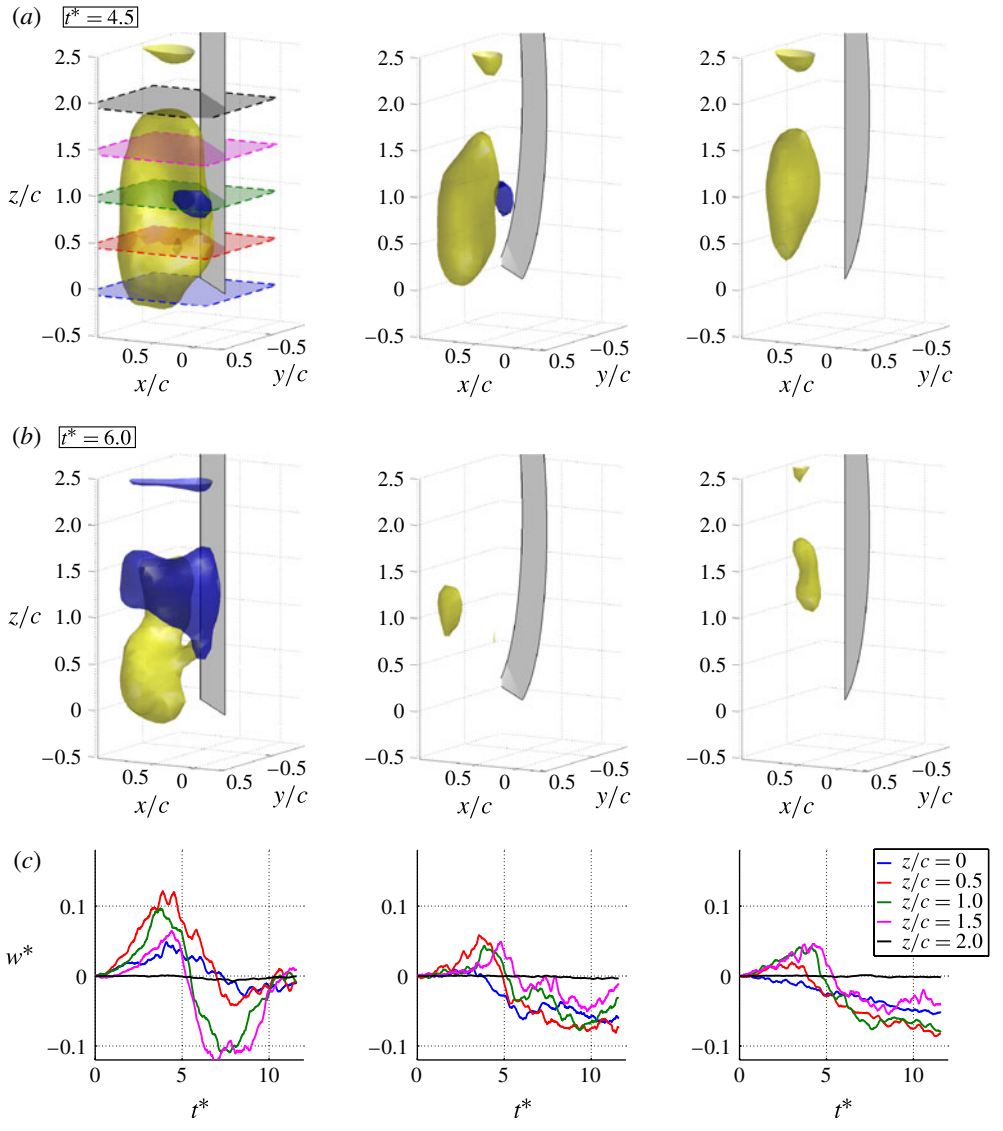


FIGURE 9. (Colour online) (*a*) Isosurfaces of inboard-directed (yellow) and outboard-directed (blue) $w^* = 0.3$ at $t^* = 4.5$ highlight the higher level of inboard-directed velocity on the rectangular planform (rectangular, lunate and truncate planforms are shown from left to right). (*b*) The arch-vortex causes a surface-normal swirling flow pattern on the rectangular planform at $t^* = 6$ similar to the flow pattern observed on an aspect-ratio two rectangular plate by Yilmaz & Rockwell (2012). This flow pattern persists in the relaxation phase (see movie S2 of the supplementary material) and is not evident on planforms with spanwise leading-edge curvature. (*c*) Time-histories of $\bar{w}^*$ highlight the suppression of inboard-directed flow on both the lunate and truncate planforms.

a growth phase, a relaxation phase, and a steady phase. During the growth phase the LEVs on all three planforms are subject to vortex compression. However, during the relaxation phase the forces and flow field vary primarily under the influence of spanwise leading-edge curvature, while the tip- and trailing-edge shapes play

https://doi.org/10.1017/jfm.2013.400 Published online by Cambridge University Press

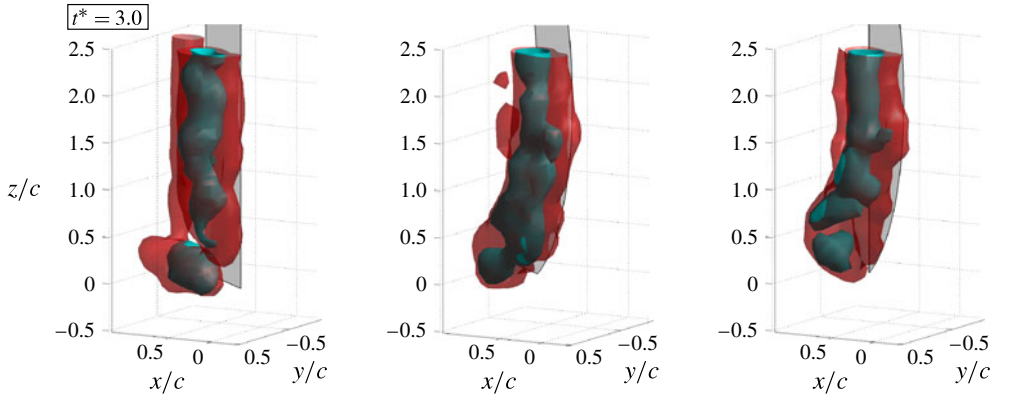


FIGURE 10. (Colour online) Regions of vortex compression are identified by isosurfaces of negative $W^*_{\parallel} = 2.5$ (light-blue) (rectangular, lunate and truncate planforms are shown from left to right). The LEV is plotted for reference via an isosurface of $|\boldsymbol{\omega}|^* = 2.5$ (red). $t^* = 3.0$. During the growth phase, the LEVs on all three planforms are subject to vortex compression.

only a minor role. Here an arch-shaped LEV develops in the absence of spanwise leading-edge curvature. This arch vortex is found to be caused by high levels of inboard-directed flow on the rectangular planform, which promotes the streamwise and surface-normal tilting of the initially spanwise-directed LEV. Conversely, outboard-directed convection of vorticity, and not vortex stretching, is found to suppress the arch-vortex formation on the lunate and truncate planforms. Finally, the vortical near-wake produced in the presence of spanwise leading-edge curvature is found to be strongly correlated with a favourable lift-to-drag ratio during the relaxation phase, in turn shedding light on the evolutionary convergence towards spanwise leading-edge curvature on biological appendages.

Supplementary movies

Supplementary movies are available at http://dx.doi.org/10.1017/jfm.2013.400.

REFERENCES

BARNES, C. & VISBAL, M. 2012 High-Ffidelity simulations of a hovering wing. *AIAA Paper* 2012-2699.

ELOY, C. 2013 On the best design for undulatory swimming. *J. Fluid Mech.* **717**, 48–89.

GAZZOLA, M., VAN REES, W. M. & KOUMOUTSAKOS, P. 2012 C-start: optimal start of larval fish. *J. Fluid Mech.* **698**, 5–18.

GRANLUND, K., OL, M. & BERNAL, L. 2011 Experiments on pitching plates: force and flowfield measurements at low Reynolds numbers. *AIAA Paper* 2011-872.

HARBIG, R. R., SHERIDAN, J. & THOMPSON, M. C. 2013 Reynolds number and aspect ratio effects on the leading-edge vortex for rotating insect wing planforms. *J. Fluid Mech.* **717**, 166–192.

HARTLOPER, C., KINZEL, M. & RIVAL, D. E. 2013 On the competition between leading-edge and tip-vortex growth for a pitching plate. *Exp. Fluids* **54**, 1447.

KINZEL, M., WOLF, M., HOLZNER, M., LUETHI, B., TROPEA, C. & KINZELBACH, W. 2011 Simultaneous two-scale 3D-PTV measurements in turbulence under the influence of system rotation. *Exp. Fluids* **51**, 75–82.

https://doi.org/10.1017/jfm.2013.400 Published online by Cambridge University Press

LENTINK, D. & DICKINSON, M. H. 2009 Rotational accelerations stabilize leading edge vortices on revolving fly wings. *J. Expl Biol.* **212**, 2705–2719.

LIGHTHILL, M. J. 1969 Hydromechanics of aquatic animal propulsion. *Annu. Rev. Fluid Mech.* **1**, 413–446.

LUETHI, B., TSINOBER, A. & KINZELBACH, W. 2005 Lagrangian measurement of vorticity dynamics in turbulent flow. *J. Fluid Mech.* **528**, 87–118.

MAXWORTHY, T. 2007 The formation and maintenance of a leading-edge vortex during the forward motion of an animal wing. *J. Fluid Mech.* **587**, 471–475.

TAIRA, K. & COLONIUS, T. 2009 Three-dimensional flows around low-aspect-ratio flat-plate wings at low Reynolds numbers. *J. Fluid Mech.* **623**, 187–207.

TRIANTAFYLLOU, M. S. 2012 Survival hydrodynamics. *J. Fluid Mech.* **698**, 1–4.

VISBAL, M., YILMAZ, T. & ROCKWELL, D. 2013 Three-dimensional vortex formation on a heaving low-aspect-ratio wing: computations and experiments. *J. Fluid Struct.* **38**, 58–76.

YILMAZ, T. O. & ROCKWELL, D. 2012 Flow structure on finite-span wings due to pitch-up motion. *J. Fluid Mech.* **691**, 518–545.

https://doi.org/10.1017/jfm.2013.400 Published online by Cambridge University Press